

## ARTICLE

<https://doi.org/10.1038/s42005-019-0258-x>

OPEN

# Metasurface zone plate for light manipulation in vectorial regime

Gwanho Yoon <sup>1</sup>, Jaehyuck Jang<sup>2</sup>, Junggho Mun <sup>2</sup>, Ki Tae Nam <sup>3</sup> & Junsuk Rho <sup>1,2,4\*</sup>

Fresnel zone plates consisting of multiple concentric rings have been realized by tailoring amplitude, phase and polarization of light, but conventional Fresnel zone plates require totally different materials to control each property reducing light controllability. Here, a metasurface zone plate in which rings are composed of subwavelength antenna arrays is proposed to individually control amplitude, phase and polarization by the consistent material platform of metasurfaces. Hence, versatile degrees of freedom can be achieved to focus electromagnetic waves. We verify that dielectric metasurfaces can generate arbitrary polarization states to cover the whole Poincaré sphere in the visible regime, allowing light manipulation in the vectorial regime, which is not feasible by a conventional single liquid crystal film. Experimental demonstration of a polarization-modulated metasurface zone plate confirms the functional capability of dielectric metasurfaces exhibiting higher focusing efficiency than amplitude-modulated zone plates.

<sup>1</sup>Department of Mechanical Engineering, Pohang University of Science and Technology (POSTECH), Pohang 37673, Republic of Korea. <sup>2</sup>Department of Chemical Engineering, Pohang University of Science and Technology (POSTECH), Pohang 37673, Republic of Korea. <sup>3</sup>Department of Materials Science and Engineering, Seoul National University, Seoul 08826, Republic of Korea. <sup>4</sup>National Institute of Nanomaterials Technology (NINT), Pohang 37673, Republic of Korea. \*email: [jsrho@postech.ac.kr](mailto:jsrho@postech.ac.kr)

**A** Fresnel zone plate (FZP) is a diffractive lens that consists of a series of concentric, alternating opaque and transparent rings<sup>1</sup>. Conventional refractive lenses generate a quadratic wavefront to focus transmitted light on a focal point, but the FZP induces constructive interference of transmitted light at its focal point by modulating light at particular positions of the rings. FZPs have many applications in the visible such as subwavelength imaging<sup>2</sup>, achromatic focusing<sup>3,4</sup>, fluorescence microscopy<sup>5,6</sup>, optical lithography<sup>7</sup>, and gunsight technology<sup>8</sup>. Furthermore, FZPs can operate in a particular wavelength range where refractive systems fail. For example, the FZP is the indispensable focusing element in X-ray optics because most materials have near-unity refractive indices in X-ray regime<sup>9</sup>. In addition to electromagnetic (EM) waves, FZPs can also focus other waves such as acoustic waves<sup>10</sup> and Broglie matter waves<sup>11</sup>.

FZPs have been realized by tailoring wave properties such as amplitude, phase, and polarization, but conventional FZPs require totally different materials to control each property, which reduces degrees of freedom (DOF) in a functional multiplicity. Typical amplitude FZPs require opaque material to block the incident light and achieve constructive interference at the focal point. Phase FZPs require transparent materials to adjust phase delay at each position<sup>12</sup>. Due to the additional phase shift, transmitted light from the phase-shift region can constructively interfere with transmitted light from the bare region, increasing the focusing efficiency depending on the amount of the phase shift. Polarization FZPs use anisotropic materials such as liquid crystals (LCs) to manipulate polarization<sup>13,14</sup>. Light rays of orthogonal polarizations do not interfere with each other; therefore, the focusing efficiency of polarization FZPs becomes double of amplitude FZPs by converting incident polarization to its orthogonal state. However, arbitrary polarization generation is not feasible by a single layer of the conventional LC film disturbing perfect vectorial modulation.

Metasurfaces that are composed of subwavelength antenna arrays can be promising functional elements to replace conventional thin film-based rings of the FZP for the functional multiplicity. Subwavelength antennas develop strong EM resonances, so the transmission amplitude, phase, and polarization can be modulated by adjusting the shape and arrangement of antennas<sup>15–20</sup>, exhibiting many applications such as lenses<sup>21–24</sup>, holograms<sup>25–30</sup>, polarizers<sup>17,31,32</sup>, beam splitters<sup>33</sup>, optical isolators<sup>34</sup>, and color filters<sup>35</sup>. In this article, we designate FZPs in which thin film-based rings are replaced with metasurfaces as metasurface zone plates (MZPs) to distinguish them from conventional thin film-based FZPs. Amplitude MZPs have been demonstrated verifying the functional improvement. For example, achromatic focusing was achieved by tailoring transmission spectra of antennas<sup>36,37</sup>. Anisotropic antennas in which transmittance varies with polarization direction have controllable focal points by polarizations<sup>38,39</sup>. Although reported MZPs have been realized by the amplitude control only, they show a potential advance over conventional FZPs.

Here, we develop MZPs that can individually control the amplitude, phase, and polarization of light by the same material platform of metasurfaces for the functional multiplicity. Arbitrary polarization control by metasurfaces is investigated to verify the capability of MZPs because full-range amplitude and phase modulations have been already demonstrated by other reported works<sup>40–42</sup>. We confirm that dielectric metasurfaces can generate arbitrary polarization states to cover the whole Poincaré sphere in the visible allowing light manipulation in vectorial regime, which is not feasible by the conventional single LC film. Experimental demonstration of a polarization MZP verifies the polarization controllability of dielectric metasurfaces. To account for the polarization effect, interference conditions at the focal point are

analyzed in vectorial regime to relate functions of metasurfaces to the focusing efficiency, and ideally, the polarization MZP is expected to have twice the efficiency of amplitude FZPs. High cross-polarization and low co-polarization transmittances are required for the polarization MZP at a target wavelength  $\lambda = 635$  nm. The transmission requirement can be satisfied by dielectric nanorods because they can induce strong magnetic dipole resonances that are 180° out of phase by two linearly polarized light incidence. The MZP is composed of hydrogenated amorphous silicon (a-Si:H), and the FZP is fabricated using chromium (Cr) thin film to compare focusing and imaging characteristics. The MZP is designed by the same formula of the FZP. The MZP benefits from ~1.5 times higher focusing efficiency as well as ~2.3 times higher imaging contrast than the FZP. Since metasurface-based rings of MZPs can provide more DOF to fit one's demand compared with simple thin film-based rings, which limit the functionality of FZPs, MZPs can find applications of multifunctional light-focusing devices replacing conventional thin film-based FZPs.

## Results

**Focusing characteristics of MZP.** FZPs consist of several thin film-based rings (Fig. 1a), whereas MZPs are composed of nanostructured rings, which allow individual control of amplitude, phase and polarization (Fig. 1b). The focusing characteristics of MZPs are investigated using vectorial analysis of transmitted light (Fig. 2a). Typical FZPs can be divided into two regions of opaque rings and transparent rings. The  $n$ th ring has an outer radius of<sup>43</sup>

$$r_n = \sqrt{n\lambda_d \left( f + \frac{n\lambda_d}{4} \right)}, \quad (1)$$

where  $n$  is an integer,  $\lambda_d$  is a design wavelength, and  $f$  is a focal length. In this work, the maximum integer  $N = 46$ ,  $\lambda_d = 635$  nm, and  $f = 2$  mm are used for both the FZP and MZP. At the focal point, transmitted light from neighbored rings has  $\pi$ -phase difference, so constructive interference can be achieved by blocking

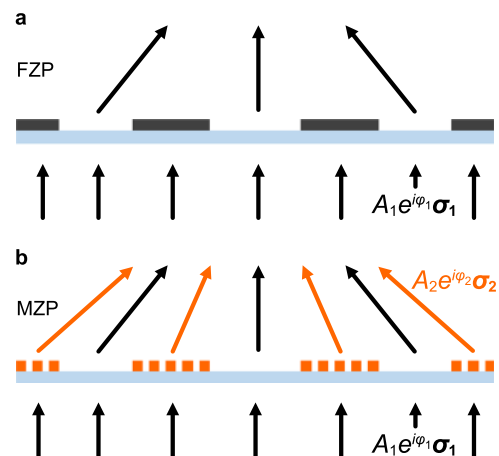


**Fig. 1 Schematics of Fresnel zone plates (FZPs) and metasurface zone plates (MZPs).** **a** The FZP controls wave properties such as transmission amplitude to focus light. By blocking transmission at particular positions, constructive interference occurs at the focal point. **b** The MZP has functional elements of metasurfaces instead of opaque rings for the vectorial modulation. Since the metasurface can individually control transmission amplitude, phase, and polarization, the MZP provides more degrees of freedom for the functional multiplicity than the FZP.  $\sigma_i$  represent arbitrary Jones vectors,  $A$  and  $\varphi$  are arbitrary amplitude and phase, respectively.

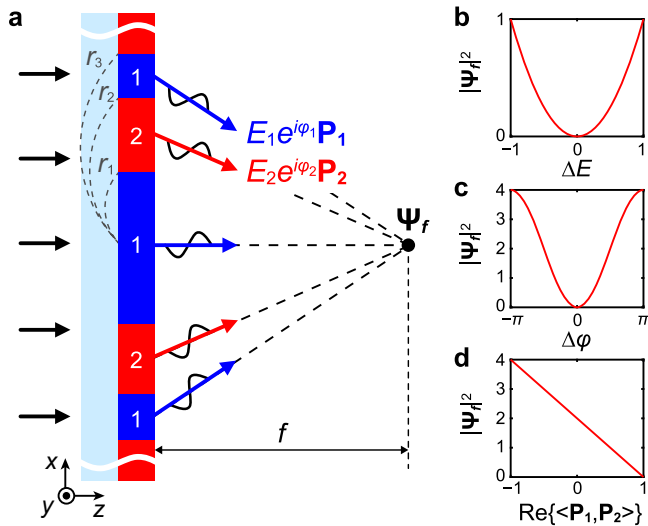


**Fig. 2** Vectorial analysis of light focusing by metasurface zone plates (MZPs). **a** Cross section of the MZP that has the same ring radii  $r_n$  as the Fresnel zone plate. Black arrows: incident plane waves into the MZP; blue arrows: transmitted waves through the region 1; red arrows: transmitted waves through the region 2;  $E_i$ : electric field amplitudes;  $\varphi_i$ : phases;  $\mathbf{P}_i$ : normalized arbitrary Jones vectors;  $f$ : a focal length. Boldface texts represent vector quantities, and dashed lines are guides. The complex vectorial amplitude  $\Psi_f$  at the focal point varies depending on the transmission condition from each region. **b-d** Focal spot intensity variation by **(b)** amplitude, **(c)** phase and **(d)** polarization modulation.  $\Delta E = E_1 - E_2$ : amplitude difference;  $\Delta\varphi = \varphi_1 - \varphi_2$ : phase difference. Transmitted amplitudes from both regions are normalized to unity for the phase modulation and polarization modulation cases.

either odd-numbered or even-numbered rings. The Babinet’s principle states that the interchange of the two regions does not affect the focusing properties<sup>44</sup>. The MZP also has two regions (1 and 2) in which boundaries coincide with the FZP. The outer radius of the  $n$ th ring of the MZP is also expressed by Eq. 1. For the two regions, two-dimensional complex amplitudes  $\Psi_1$  and  $\Psi_2$  right after the MZP can be described as

$$\Psi_1 = E_1 e^{i\varphi_1} \mathbf{P}_1, \tag{2}$$

$$\Psi_2 = E_2 e^{i\varphi_2} \mathbf{P}_2, \tag{3}$$

where  $E_i$  are electric field amplitudes,  $\varphi_i$  are phases, and  $\mathbf{P}_i$  are normalized arbitrary Jones vectors of transmitted waves from each region. Boldface texts represent vector quantities. Therefore, the complex amplitude  $\Psi_f$  at the focal point becomes

$$\Psi_f = E_1 e^{i\varphi_1} \mathbf{P}_1 + E_2 e^{i(\varphi_2 + \pi)} \mathbf{P}_2, \tag{4}$$

accounting for the additional  $\pi$  phase shift in neighbored rings (Eq. 1). The intensity at the focal point can be represented as

$$|\Psi_f|^2 = E_1^2 + E_2^2 - 2E_1 E_2 \text{Re}\left\{ e^{i(\varphi_1 - \varphi_2)} \langle \mathbf{P}_1, \mathbf{P}_2 \rangle \right\}, \tag{5}$$

where  $\text{Re}\{\cdot\}$  denotes a real part of a complex value, and the intensity at the focal point is strongly related to the focusing efficiency.

Amplitude MZPs modulate transmission amplitude, while transmission phase and polarization from two regions remain constant. The intensity at the focal point is described as

$$|\Psi_f|^2 = (E_1 - E_2)^2, \tag{6}$$

because the complex values in Eq. 5 become unity. Therefore, the focusing efficiency increases as the transmission amplitude

difference increases (Fig. 2b). Normalization of the amplitude of the incident wave yields the maximum intensity of 1 when one region is perfectly opaque, and the other region is transparent.

Phase MZPs modulate the transmission phase of two regions maintaining constant transmission amplitude and polarization. The intensity at the focal point is

$$|\Psi_f|^2 = 2 - 2\cos(\varphi_1 - \varphi_2), \tag{7}$$

with the normalization of incident field. Depending on the phase difference, the intensity varies from 0 to 4, which is much higher than in the amplitude MZP (Fig. 2c). The intensity is maximized when the phase difference becomes  $\pi$ .

Polarization MZPs modulate transmission polarization, while the amplitude and phase remain constant. The intensity at the focal point becomes

$$|\Psi_f|^2 = 2 - 2\text{Re}\{\langle \mathbf{P}_1, \mathbf{P}_2 \rangle\}, \tag{8}$$

with the normalized incident field.  $\text{Re}\{\langle \mathbf{P}_1, \mathbf{P}_2 \rangle\}$  represents similarity of the two polarization states. Since the Jones vectors are normalized to have unity magnitude,  $-1 \leq \text{Re}\{\langle \mathbf{P}_1, \mathbf{P}_2 \rangle\} \leq 1$  (Fig. 2d). It is worth noting that negative values of this term are just positive counterparts with  $\pi$  phase shift. Therefore, if the phase-shift effect is eliminated,  $0 \leq \text{Re}\{\langle \mathbf{P}_1, \mathbf{P}_2 \rangle\} \leq 1$ . When  $\text{Re}\{\langle \mathbf{P}_1, \mathbf{P}_2 \rangle\} = 0$ , the two polarizations are orthogonal to each other, and the intensity at the focal point becomes 2, which is twice the intensity of amplitude FZPs.

**Design of polarization MZP.** To realize the MZP that operates in orthogonal polarization mode, metasurface rings of the MZP should have high cross-polarization and zero co-polarization transmittance. Dielectric building blocks can satisfy this condition because incident optical waves induce strong electric and magnetic resonances inside dielectric antennas. Since the polarization conversion efficiency can be drastically increased by tailoring the resonance conditions<sup>23</sup>, the dielectric metasurface is suitable for the polarization MZP. The a-Si:H nanorods are exploited to realize the MZP that satisfies the orthogonality condition. Pure amorphous silicon has a high refractive index, but suffers from considerable optical loss in visible wavelengths<sup>45</sup>. The extinction coefficient of crystalline silicon is low enough in the visible, but it is not feasible to deposit crystalline silicon on a glass substrate due to lattice constant mismatch. In contrast, the a-Si:H can be easily deposited on a glass substrate by plasma-enhanced chemical vapor deposition. The extinction coefficient of the a-Si:H is as low as that of crystalline silicon because the hydrogen atoms in a-Si:H reduce the defect density of the pure amorphous silicon<sup>46</sup> (Supplementary Fig. 1). Therefore, the intrinsic optical loss can be minimized in strong electric or magnetic resonances induced inside a-Si:H antennas.

Rigorously coupled wave analysis demonstrates that a-Si:H antennas can closely approach the orthogonality condition at  $\lambda = 635$  nm. Linearly polarized light is normally incident from the glass substrate to the a-Si:H antenna (Fig. 3a), and two polarization directions each yields a transmission coefficient. The transmission coefficients of linearly polarized light can be used to derive the transmission response of circularly polarized light (Fig. 3b, c). When a left-handed circularly polarized light is incident on the antenna, the Jones vector of transmitted wave can be expressed as<sup>47</sup>

$$\frac{T_L + T_S}{2} \begin{bmatrix} 1 \\ i \end{bmatrix} + \frac{T_L - T_S}{2} e^{i2\alpha} \begin{bmatrix} 1 \\ -i \end{bmatrix}, \tag{9}$$

where  $T_L$  and  $T_S$  represent complex transmission coefficients along the long and short axis of the antenna, respectively, and  $\alpha$  is

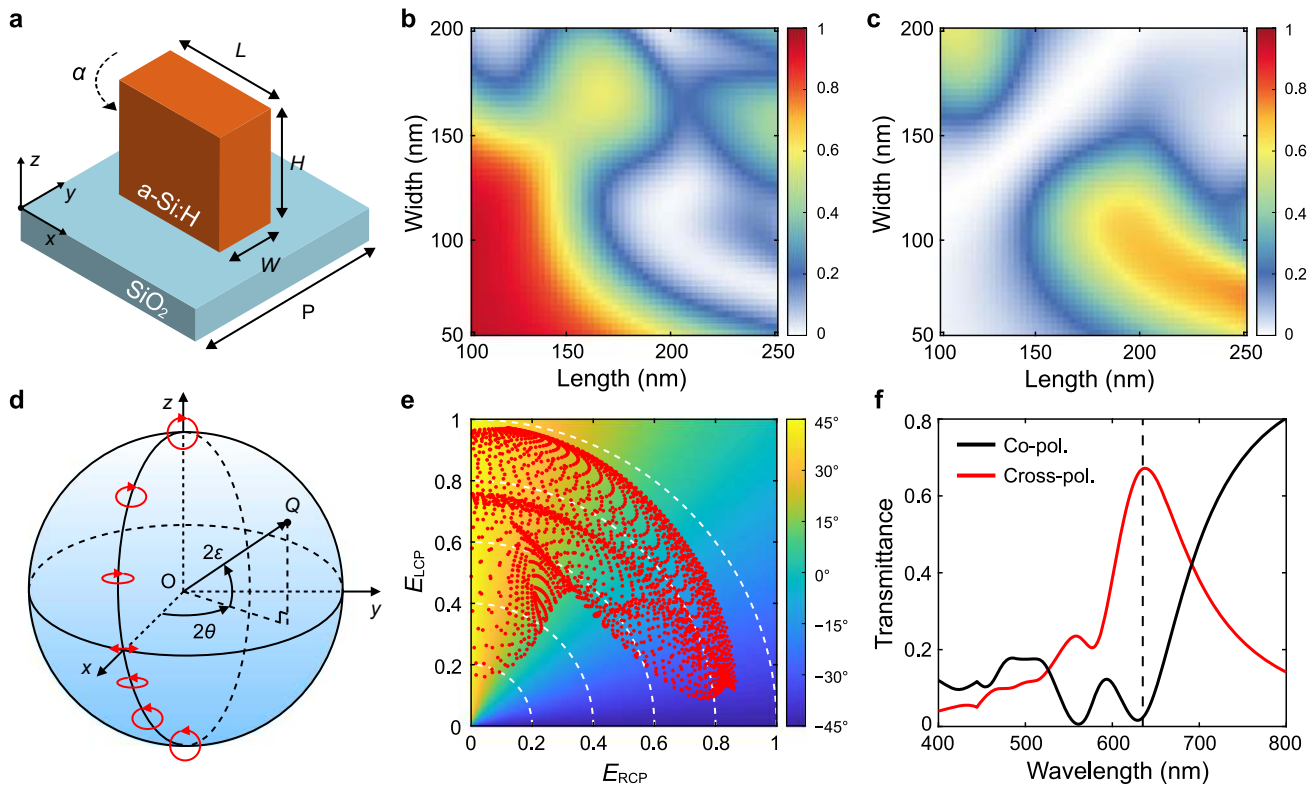


**Fig. 3 Simulation of the polarization states that can be achieved by dielectric metasurfaces.** **a** Unit cell configuration of the hydrogenated amorphous silicon (a-Si:H) rectangular antenna in which length  $L = 190$  nm; width  $W = 100$  nm; height  $H = 330$  nm; pitch  $P = 300$  nm.  $\alpha$  is the antenna rotation angle. **b, c** Calculated transmittances of co-polarization and cross-polarization components, respectively. Length varies from 100 to 250 nm, and corresponding width varies from 50 to 200 nm. Calculated values are normalized to the incident field. **d** The Poincaré sphere that represents an arbitrary polarization state as a point  $Q$  on the surface. To cover the whole surface, longitude  $2\theta$  and latitude  $2\varepsilon$  of the point should have ranges of  $0^\circ \leq 2\theta \leq 360^\circ$  and  $-90^\circ \leq 2\varepsilon \leq 90^\circ$ , respectively. Red circles and lines indicate schematics of polarization ellipses at each position. **e** Calculation of  $\varepsilon$  by using the normalized amplitudes of transmitted left-handed circular-polarization ( $E_{LCP}$ ) and right-handed circular-polarization ( $E_{RCP}$ ) components. Red dots represent calculated transmission amplitude plots from **b** and **c**. White dashed curves indicate transmittance contours to guide the eye. **f** Calculated co-polarization and cross-polarization transmittance of the unit structure in which length is 190 nm and width is 100 nm. The dashed line indicates a location of  $\lambda = 635$  nm. The co-polarization transmittance is suppressed as almost zero, while the high cross-polarization transmittance is achieved at  $\lambda = 635$  nm.

the antenna rotation angle along the  $z$ -axis. The first term indicates the co-polarization component, while the second term represents the cross-polarization component. The polarization state of the transmitted wave can be represented on the Poincaré sphere as a point with a certain longitude  $2\theta$  and latitude  $2\varepsilon$  (Fig. 3d). To cover the whole surface of the sphere,  $\theta$  and  $\varepsilon$  should have ranges of  $0^\circ \leq \theta \leq 180^\circ$  and  $-45^\circ \leq \varepsilon \leq 45^\circ$ , respectively. The polarization ellipse orientation  $\theta$  is determined by relative phase difference of the two circular-polarization components. Since the relative phase difference can be controlled by adjusting  $\alpha$  (Eq. 9), the requirement of  $\theta$  can be satisfied. The axis ratio  $\varepsilon$  of the polarization ellipse can be expressed as

$$\varepsilon = \cot^{-1} \left( \frac{E_{LCP} + E_{RCP}}{E_{LCP} - E_{RCP}} \right), \quad (10)$$

where  $E_{LCP}$  and  $E_{RCP}$  represent the amplitude of left-handed circular-polarization and right-handed circular-polarization components, respectively. The calculation results show that dielectric nanostructures can achieve nearly the required range of  $-45^\circ \leq \varepsilon \leq 45^\circ$  by adjusting the length and width with the fixed height of 330 nm and pitch of 300 nm (Fig. 3e). Therefore, transmitted polarization states from our metasurface cover the whole surface of the Poincaré sphere allowing arbitrary polarization control, and thereby MZPs can provide more DOF than conventional polarization FZPs based on LCs. The

polarization conversion efficiency is the modulus square of the second term in Eq. (9), and the optimized structure achieves both high cross-polarization and near-zero co-polarization transmittances (Fig. 3f).

The electric and magnetic fields around the optimized antenna are analyzed to identify the origin of the high polarization conversion efficiency. When  $x$ -polarized light is incident to the antenna, a very strong magnetic dipole resonance appears along the  $y$ -axis inside the antenna (Fig. 4a). In the case of  $y$ -polarized light incidence, a magnetic dipole resonance is still dominant along the  $x$ -axis (Fig. 4b). Therefore, transmission characteristics of the antenna can be related to the magnetic dipole resonance properties. Multipole expansion analysis from the electric and magnetic fields is also performed to achieve more quantitative analysis on the magnetic dipole resonances<sup>48</sup>. For both  $x$ - and  $y$ -polarized light incidence, the scattering cross-section coefficient of the magnetic dipole resonance is larger than the sum of the other three major resonances of the electric dipole, electric quadrupole and magnetic quadrupole at  $\lambda = 635$  nm (Fig. 4c, d). This result coincides with the appearance of the electric and magnetic field distributions around the antenna. Furthermore, the magnetic dipole resonances induced by each polarization have  $\sim \pi$ -phase difference at  $\lambda = 635$  nm. It means that the antenna acts as a half-wave plate removing the co-polarization transmission (Eq. 9).



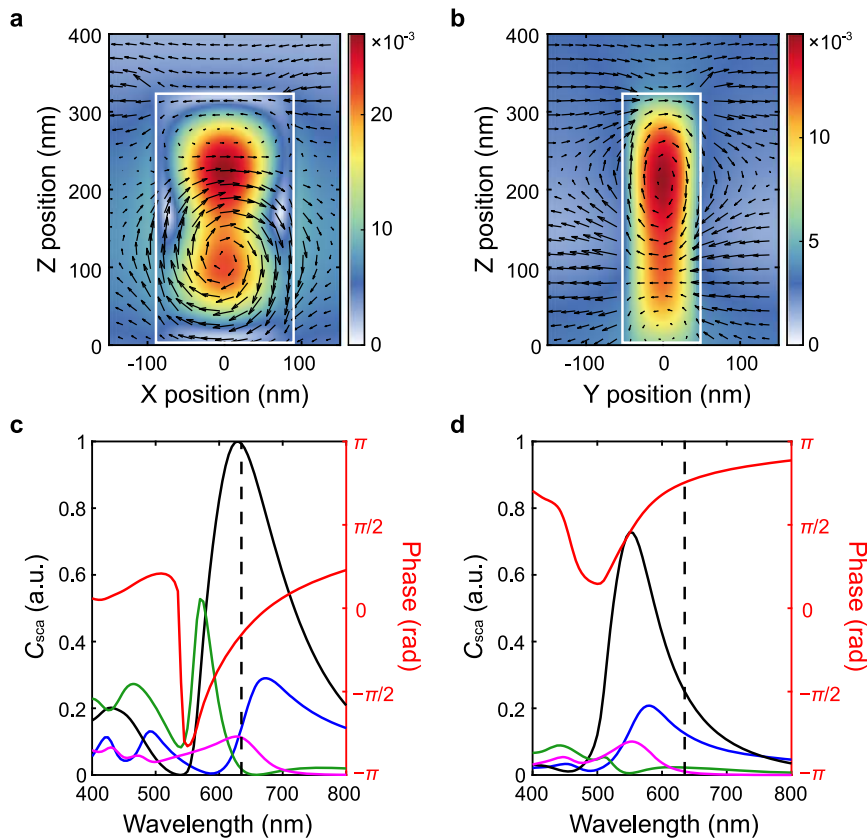


**Fig. 4 Electromagnetic responses of the unit structure.** **a, b** Magnetic field amplitude distributions under **a** x-polarized light incidence and **b** y-polarized light incidence. Black arrows: electric field magnitude and direction. White lines: boundaries of the unit structure to guide eyes. All field intensities are normalized to the incident field amplitude. Due to rotational electric fields, we can estimate that the magnetic dipole resonance is dominant for both polarizations. **c, d** Calculated scattering cross-section coefficients ( $C_{sca}$ ) by the multipole expansion analysis under **c** x-polarized light incidence and **d** y-polarized light incidence. Each colored line represent the coefficient of the electric dipole (blue), magnetic dipole (black), electric quadrupole (green) and magnetic quadrupole (magenta) resonance modes. Red lines: phase of magnetic dipole modes; black dashed lines: location of  $\lambda = 635$  nm. All coefficients are normalized to the maximum value of the magnetic dipole resonance under x-polarization incidence. In both cases, the magnetic dipole resonance is dominant at  $\lambda = 635$  nm with  $-\pi$ -phase difference, so the structure acts as a half-wave plate that yields the perfect polarization conversion.

**Experimental demonstration of polarization MZP.** The fabricated MZP demonstrates  $\sim 1.5$  times higher focusing efficiency than the conventional FZP. The FZP is fabricated using a 100-nm-thick Cr thin film to compare the focusing efficiencies (Fig. 5a, b). They have the same configuration except that the MZP has the dielectric metasurface rings (Fig. 5c–e), whereas the FZP consists of Cr rings. Transmission and focusing characteristics are evaluated by illuminating them with circularly polarized light of  $\lambda = 635$  nm (Supplementary Fig. 2a). The FZP looks like a reversed optical micrograph at  $z = 0$  mm due to zero transmission through the Cr thin film (Fig. 5f). When the analyzer rotates by  $90^\circ$ , all images disappear because transmitted light from the FZP is blocked by the analyzer (Fig. 5g). The MZP looks the same as the FZP without the analyzer rotation (Fig. 5h). Dark rings are caused by polarization conversion from the metasurface. In contrast to the FZP, images still appear in the MZP when the analyzer is rotated by  $90^\circ$ . The reversed image contrast confirms the polarization conversion by the metasurface (Fig. 5i). Without the analyzer, all images from the MZP look like a superposition of the co-polarization and cross-polarization images (Fig. 5j). Constructive interference by transmitted light occurs at the focal length of  $z = 2$  mm for both the FZP and MZP (Fig. 5k–o). The focusing efficiency can be calculated as the ratio of the measured optical power of the focal spot to the total incident optical power.

The experimentally measured focusing efficiencies are 10% for the FZP and 14.6% for the MZP, which consists of 10% co-polarization and 4.6% cross-polarization powers. The experimental polarization conversion efficiency of the metasurface is 46%, which is lower than the theoretical value of 67% due to suboptimal fabrication of the MZP.

The focal spot of the MZP has the same size, but  $\sim 1.5$  times higher intensity than that of the FZP (Fig. 6a, b). Since the analyzer is removed from the optical setup, the focal spot intensity should be proportional to the focusing efficiency (Supplementary Fig. 2b). The full-width at half-maximum (FWHM) of the focal spot of the FZP can be calculated as<sup>43</sup>

$$\text{FWHM} = \Delta r, \quad (11)$$

where  $\Delta r$  represents the width of the outermost zone. When  $\Delta r$  is much smaller than the total radius of the FZP, the FWHM can be described as

$$\text{FWHM} \approx \frac{\lambda_d f}{2r_N} = \frac{\lambda_d f}{2} \left[ N \lambda_d \left( f + \frac{N \lambda_d}{4} \right) \right]^{-\frac{1}{2}} \approx 2.6 \mu\text{m}, \quad (12)$$

which agrees well with the measured value of  $\sim 2.8 \mu\text{m}$  for both the MZP and FZP (Fig. 6c).

The MZP captures higher image contrast than the FZP does (Fig. 6d–f). A typical negative-type 1951 United States Air Force

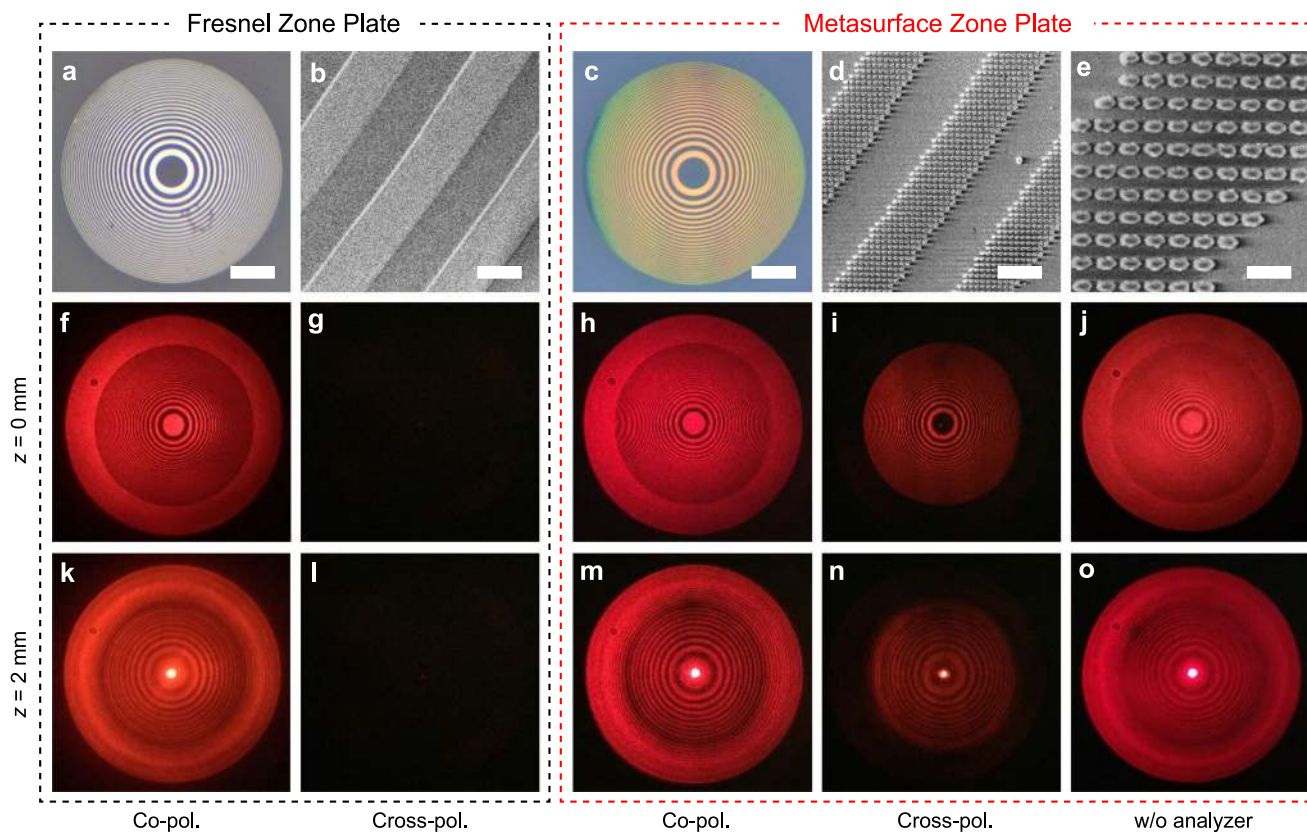


**Fig. 5 Images of the Fresnel zone plate (FZP) and metasurface zone plate (MZP).** **a** Optical micrograph of the FZP. A 100-nm-thick chromium (Cr) thin film is used as opaque rings. Scale bar: 100  $\mu\text{m}$ . **b** Scanning electron micrograph (SEM) of the FZP. Scale bar: 2  $\mu\text{m}$ . **c** Optical micrograph of the MZP that consists of silicon metasurfaces. Scale bar: 100  $\mu\text{m}$ . **d** SEM of the MZP. Scale bar: 2  $\mu\text{m}$ . **e** Magnified SEM of the MZP. Scale bar: 500 nm. **f–o** Transmission images at **f–j**  $z = 0$  mm and **k–o**  $z = 2$  mm using a monochromatic laser of  $\lambda = 635$  nm.  $z$  represents a distance from the zone plate along the optical axis. Co-polarization and cross-polarization imaging can be switched according to the rotation angle of the analyzer. In co-polarization imaging at  $z = 0$  mm, dark areas of the FZP result from zero transmission by Cr rings, but dark areas of the MZP result from polarization conversion by metasurfaces. In cross-polarization imaging, no light can pass through the analyzer in the FZP, whereas cross-polarized light from the MZP can pass through the analyzer, so contrast-reversed images appear. The co-polarization focusing efficiency is 10% for both the FZP and MZP, and the MZP has additional cross-polarization focusing efficiency of 4.6%. Therefore, the MZP has  $\sim 1.5$  times higher focusing efficiency than the FZP.

resolution test chart is used as the imaging target (Supplementary Fig. 2c). We define the image contrast as

$$C = \left| \frac{I_H - I_L}{I_L} \right|, \quad (13)$$

where  $I_H$  is the highest intensity of the image, and  $I_L$  is the lowest intensity. The FZP has  $C = 111$  whereas the MZP has  $C = 254$ , which is  $\sim 2.3$  times higher than that of the FZP.

## Discussion

The major advantage of the MZP over conventional metalenses is a high DOF to design multifunctional devices. Since metalenses are full of structures with fixed rotation angles to focus light, the number of controllable parameters for the multifunctional operation is limited resulting trade-offs. In contrast, the MZP still has several extra parameters such as structure rotation and interpolation that can be adjusted without functional degradation. In this work, all structures of the MZP have the same orientation to match the focal length of co-polarization and cross-polarization. If the orientation of each structure is adjusted, the cross-polarization function can be further controlled, while the co-polarization function is maintained. For example, transmitted cross-polarized light can have different focal lengths, propagate

without focusing, and even generate holograms. Additional structure interpolation can also allow flexible designs, especially to correct chromatic aberration. The interpolation of well-designed structures can realize achromatic light focusing by compensating diffractive dispersion.

In conclusion, we propose the concept of the MZP that replaces thin film-based rings of the FZP with functional elements of metasurfaces. The MZP allows to individually control amplitude, phase, and polarization by the same material platform of metasurfaces, whereas conventional thin film-based FZPs require different materials to control each property. Dielectric metasurfaces can generate arbitrary polarization states, and we experimentally demonstrate the polarization MZP to focus light by the pure polarization control. At  $\lambda = 635$  nm, a-Si:H nanorods strongly confine magnetic dipole resonances with  $\sim \pi$ -phase difference, and thereby achieve high cross-polarization and zero co-polarization transmittance. The fabricated MZP shows  $\sim 1.5$  times higher focusing efficiency as well as  $\sim 2.3$  times higher image contrast than the typical FZP based on the Cr thin film. Since metasurface-based rings provide high DOF for the functional multiplicity, the MZP is favorable to realize ultrathin multifunctional light-focusing devices replacing conventional thin film-based FZPs.

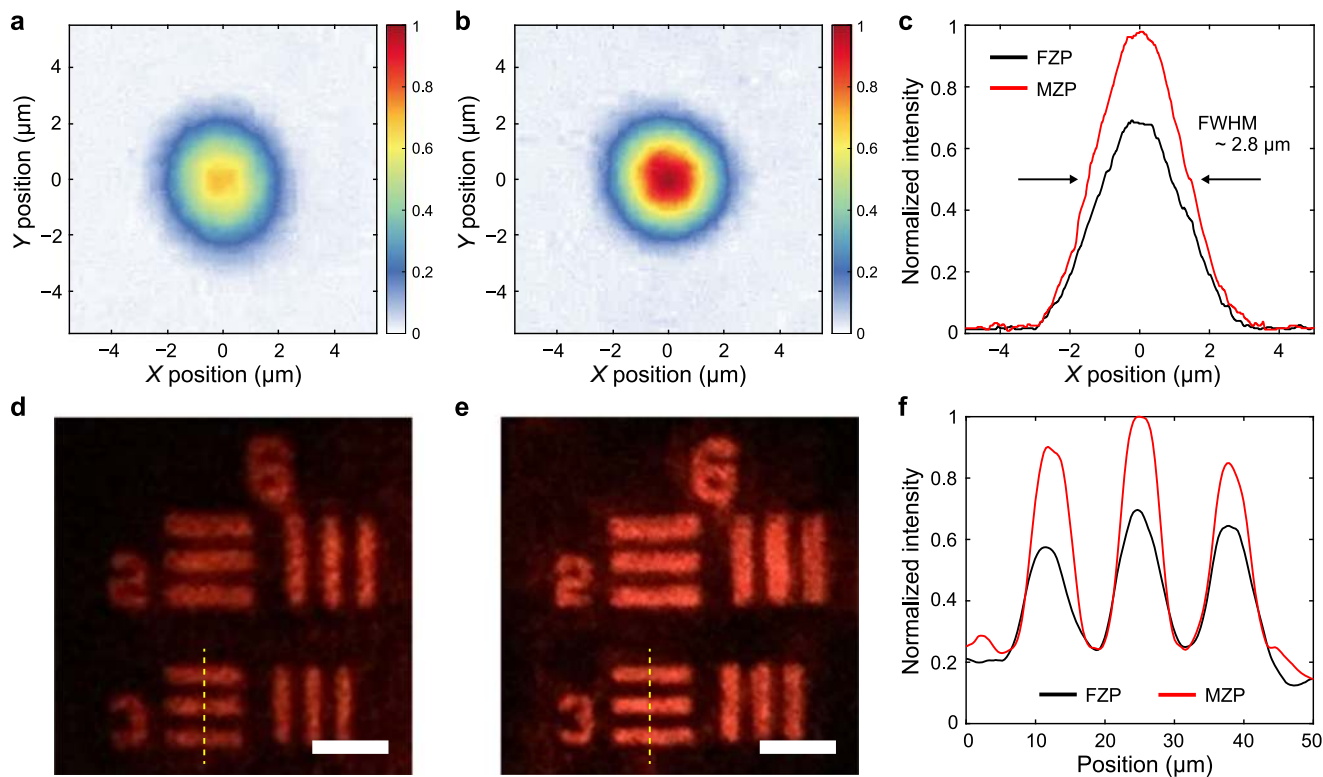


**Fig. 6 Characterization of the focal spot and image contrast.** **a, b** Focal spot images captured by a camera without the analyzer at the focal point of **a** the Fresnel zone plate (FZP) and **b** the metasurface zone plate (MZP). Spatial intensities are normalized to the maximum intensity of the MZP. **c** Comparison of the intensities at the cross section of  $-5 \mu\text{m} \leq x \leq 5 \mu\text{m}$  and  $y = 0 \mu\text{m}$ . The MZP has  $\sim 1.5$  times higher focal spot intensity than the FZP, and both focal spots have the same full-width at half-maximum (FWHM) of  $\sim 2.8 \mu\text{m}$ , which agrees with the theoretical value of  $\sim 2.6 \mu\text{m}$ . **d, e** Target imaging results by using **d** FZP and **e** MZP as each objective lens. The image contrast of the MZP is  $\sim 2.3$  times higher than that of the FZP. Scale bars:  $30 \mu\text{m}$ . **f** Comparison of normalized intensities at the cross section of yellow dashed lines in **d, e**.

## Methods

**Fabrication of FZP.** Electron beam resist (EL8, Micro Chem) was spin coated by 5000 rpm. for 60 s on a fused silica substrate, and then the sample was baked at  $150^\circ\text{C}$  for 300 s. Another resist (495 PMMA A2, Micro Chem) was spin coated by 2000 rpm. for 60 s on the sample, and then the sample was baked at  $180^\circ\text{C}$  for 300 s. Conductive polymer (Espacer 300Z, Showa Denko) was spin coated by 2000 rpm. for 60 s on the sample to prevent charge accumulation. Electron beam lithography (ELS-7800, Elionix) was used to expose electron beam on the sample, and then it was immersed into a developing solution (MIBK:IPA = 1:3, Micro Chem) for 12 min at  $0^\circ\text{C}$ . Electron beam evaporation (KVE-E4000, Korea Vacuum Tech) was used to deposit a 100-nm-thick Cr thin film on the developed sample. After deposition, the sample was immersed into acetone for 60 s with sonication for lift-off.

**Fabrication of MZP.** A 330-nm-thick a-Si:H thin film was deposited on a fused silica substrate using plasma-enhanced chemical vapor deposition<sup>49</sup> (HiDep-SC, BMR). The electron beam resist (495 PMMA A2, Micro Chem) was spin coated on the sample, and then it was baked at  $180^\circ\text{C}$  for 300 s. Conductive polymer (Espacer 300Z, Showa Denko) was spin coated by 2000 rpm. for 60 s on the sample to prevent charge accumulation. Electron beam lithography (ELS-7800, Elionix) was used to expose electron beam on the sample, and then it was immersed into a develop solution (MIBK:IPA = 1:3, Micro Chem) for 12 min at  $0^\circ\text{C}$ . Electron beam evaporation (KVE-E4000, Korea Vacuum Tech) was used to deposit a 30-nm-thick Cr thin film on the developed sample. After deposition, the sample was immersed into acetone for 60 s with appropriate sonication for lift-off, and then the a-Si:H thin film was etched along the Cr mask using inductively coupled plasma reactive ion etching. Finally, the sample was immersed into Cr etchant for 2 min to remove the Cr mask residue.

## Data availability

The data that support the findings of this study are available from the corresponding author upon reasonable request.

Received: 22 June 2019; Accepted: 21 November 2019;

Published online: 12 December 2019

## References

1. Soret, J. L. Ueber die durch kreisgitter erzeugten diffraktionsphänomene. *Ann. Phys.* **232**, 99–113 (1875).
2. Rogers, E. T. F. et al. A super-oscillatory lens optical microscope for subwavelength imaging. *Nat. Mater.* **11**, 432–435 (2012).
3. Yuan, G. H., Rogers, E. T. & Zheludev, N. I. Achromatic super-oscillatory lenses with sub-wavelength focusing. *Light Sci. Appl.* **6**, e17036 (2017).
4. Kim, J. et al. Numerical and experimental study on multi-focal metallic Fresnel zone plates designed by the phase selection rule via virtual point sources. *Appl. Sci.* **8**, 449 (2018).
5. Schonbrun, E., Abate, A. R., Steinvurzel, P. E., Weitz, D. A. & Crozier, K. B. High-throughput fluorescence detection using an integrated zone-plate array. *Lab Chip* **10**, 852–856 (2010).
6. Pang, S., Han, C., Man Lee, L. & Yang, C. Fluorescence microscopy imaging with a Fresnel zone plate array based optofluidic microscope. *Lab Chip* **11**, 3698–3702 (2011).
7. Menon, R., Patel, A., Gil, D. & Smith, H. I. Maskless lithography. *Mater. Today* **8**, 26–33 (2005).
8. Wall, M. New INL gunsight technology should improve accuracy for target shooters, hunters, soldiers. *Phys.Org* (2010). Available at: <https://phys.org/news/2010-05-inl-gunsight-technology-accuracy-shooters.html>. Accessed 21 Sept 2019.
9. Chao, W., Kim, J., Rekawa, S., Fischer, P. & Anderson, E. H. Demonstration of 12 nm resolution Fresnel zone plate lens based soft x-ray microscopy. *Opt. Express* **17**, 17669–17677 (2009).
10. Stephanis, C. G. & Hampsas, G. D. Holographic acoustical lens. *J. Acoust. Soc. Am.* **63**, 860–862 (1978).
11. Rehbein, S. et al. Nanostructuring of zone plates for helium atom beam focusing. *Microelectron. Eng.* **53**, 685–688 (2000).
12. Wood, R. W. LIII. Phase-reversal zone-plates, and diffraction-telescopes. *Philos. Mag. Ser. 5* **45**, 511–522 (1898).
13. Wang, X.-Q., Srivastava, A. K., Chigrinov, V. G. & Kwok, H.-S. Switchable Fresnel lens based on micropatterned alignment. *Opt. Lett.* **38**, 1775–1777 (2013).



14. Fiala, P., Li, Y. & Dorrer, C. Investigation of focusing and correcting aberrations with binary amplitude and polarization modulation. *Appl. Opt.* **57**, 763–771 (2018).
15. Yu, N. et al. Light propagation with phase discontinuities: generalized laws of reflection and refraction. *Science* **334**, 333–337 (2011).
16. Staude, I. et al. Tailoring directional scattering through magnetic and electric resonances in subwavelength silicon nanodisks. *ACS Nano* **7**, 7824–7832 (2013).
17. Zhao, Y. & Alù, A. Tailoring the dispersion of plasmonic nanorods to realize broadband optical meta-waveplates. *Nano Lett.* **13**, 1086–1091 (2013).
18. Kim, I. et al. Outfitting next generation displays with optical metasurfaces. *ACS Photonics* **5**, 3876–3895 (2018).
19. Raeker, B. O. & Grbic, A. Compound metaoptics for amplitude and phase control of wave fronts. *Phys. Rev. Lett.* **122**, 113901 (2019).
20. Yoon, G. et al. Wavelength-decoupled geometric metasurfaces by arbitrary dispersion control. *Commun. Phys.* **2**, 129 (2019).
21. Aieta, F. et al. Aberration-free ultrathin flat lenses and axicons at telecom wavelengths based on plasmonic metasurfaces. *Nano Lett.* **12**, 4932–4936 (2012).
22. Lin, D., Fan, P., Hasman, E. & Brongersma, M. L. Dielectric gradient metasurface optical elements. *Science* **345**, 298–302 (2014).
23. Khorasaninejad, M. et al. Metalenses at visible wavelengths: diffraction-limited focusing and subwavelength resolution imaging. *Science* **352**, 1190–1194 (2016).
24. Zhan, A. et al. Low-contrast dielectric metasurface optics. *ACS Photonics* **3**, 209–214 (2016).
25. Li, Z. et al. Dielectric meta-holograms enabled with dual magnetic resonances in visible light. *ACS Nano* **11**, 9382–9389 (2017).
26. Yoon, G., Lee, D., Nam, K. T. & Rho, J. “Crypto-display” in dual-mode metasurfaces by simultaneous control of phase and spectral responses. *ACS Nano* **12**, 6421–6428 (2018).
27. Yoon, G., Lee, D., Nam, K. T. & Rho, J. Pragmatic metasurface hologram at visible wavelength: the balance between diffraction efficiency and fabrication compatibility. *ACS Photonics* **5**, 1643–1647 (2018).
28. Ansari, M. A. et al. A spin-encoded all-dielectric metahologram for visible light. *Laser Photonics Rev.* **13**, 1900065 (2019).
29. Zhang, J. et al. Plasmonic metasurfaces with 42.3% transmission efficiency in the visible. *Light Sci. Appl.* **8**, 53 (2019).
30. Kim, K., Yoon, G., Baek, S., Rho, J. & Lee, H. Facile nanocasting of dielectric metasurfaces with sub-100 nm resolution. *ACS Appl. Mater. Interfaces* **11**, 26109–26115 (2019).
31. Park, J., Kang, J.-H., Kim, S. J., Liu, X. & Brongersma, M. L. Dynamic reflection phase and polarization control in metasurfaces. *Nano Lett.* **17**, 407–413 (2017).
32. Ren, M.-X. et al. Reconfigurable metasurfaces that enable light polarization control by light. *Light Sci. Appl.* **6**, e16254 (2017).
33. Yoon, G., Lee, D., Nam, K. T. & Rho, J. Geometric metasurface enabling polarization independent beam splitting. *Sci. Rep.* **8**, 9468 (2018).
34. Kim, M. et al. A broadband optical diode for linearly polarized light using symmetry-breaking metamaterials. *Adv. Opt. Mater.* **5**, 1700600 (2017).
35. Jang, J. et al. Kerker-conditioned dynamic cryptographic nanoprints. *Adv. Opt. Mater.* **7**, 1801070 (2019).
36. Avayu, O., Almeida, E., Prior, Y. & Ellenbogen, T. Composite functional metasurfaces for multispectral achromatic optics. *Nat. Commun.* **8**, 14992 (2017).
37. Cai, H. et al. Ultrathin transmissive metasurfaces for multi-wavelength optics in the visible. *Appl. Phys. Lett.* **114**, 071106 (2019).
38. Eisenbach, O., Avayu, O., Ditskovski, R. & Ellenbogen, T. Metasurfaces based dual wavelength diffractive lenses. *Opt. Express* **23**, 3928–3936 (2015).
39. Williams, C., Montelongo, Y. & Wilkinson, T. D. Plasmonic metalens for narrowband dual-focus imaging. *Adv. Opt. Mater.* **5**, 1700811 (2017).
40. Yu, Y. F. et al. High-transmission dielectric metasurface with  $2\pi$  phase control at visible wavelengths: high-transmission dielectric metasurface with  $2\pi$  phase control at visible wavelengths. *Laser Photonics Rev.* **9**, 412–418 (2015).
41. Huang, K. et al. Silicon multi-meta-holograms for the broadband visible light: silicon multi-meta-holograms for the broadband visible light. *Laser Photonics Rev.* **10**, 500–509 (2016).
42. Lee, G.-Y. et al. Complete amplitude and phase control of light using broadband holographic metasurfaces. *Nanoscale* **10**, 4237–4245 (2018).
43. Attwood, D. *Soft X-Rays and Extreme Ultraviolet Radiation: Principles and Applications* (Cambridge University Press, Cambridge, 1999).
44. Jackson, J. D. *Classical Electrodynamics* (Wiley, New York, 1999).
45. Pierce, D. T. & Spicer, W. E. Electronic structure of amorphous Si from photoemission and optical studies. *Phys. Rev. B* **5**, 3017–3029 (1972).
46. Paul, W. & Anderson, D. A. Properties of amorphous hydrogenated silicon, with special emphasis on preparation by sputtering. *Sol. Energy Mater.* **5**, 229–316 (1981).
47. Yu, N. & Capasso, F. Flat optics with designer metasurfaces. *Nat. Mater.* **13**, 139–150 (2014).
48. Grahn, P., Shevchenko, A. & Kaivola, M. Electromagnetic multipole theory for optical nanomaterials. *N. J. Phys.* **14**, 093033 (2012).
49. Yoon, G., Lee, D. & Rho, J. Demonstration of equal-intensity beam generation by dielectric metasurfaces. *J. Vis. Exp.* **148**, e59066 (2019).

## Acknowledgements

This work is financially supported from the LGD-SNU Incubation program funded by LG Display and the National Research Foundation grants (NRF-2019R1A2C3003129, CMM-2019M3A6B3030637, NRF-2019R1A5A8080290, NRF-2018M3D1A1058998, NRF-2015R1A5A1037668) funded by the Ministry of Science and ICT (MSIT), Republic of Korea.

## Author contributions

J.R. and G.Y. conceived the idea and initiated the project. G.Y. designed and fabricated the devices. G.Y. did optical experiments. J.J. and J.M. performed multipole expansion analysis. G.Y. analyzed the result of multipole expansion analysis. K.T.N. provided materials characterizations. G.Y. wrote the manuscript. All authors discussed the results and confirmed the final manuscript. J.R. guided the entire project.

## Competing interests

The authors declare no competing interests.

## Additional information

**Supplementary information** is available for this paper at <https://doi.org/10.1038/s42005-019-0258-x>.

**Correspondence** and requests for materials should be addressed to J.R.

**Reprints and permission information** is available at <http://www.nature.com/reprints>

**Publisher's note** Springer Nature remains neutral with regard to jurisdictional claims in published maps and institutional affiliations.



**Open Access** This article is licensed under a Creative Commons Attribution 4.0 International License, which permits use, sharing, adaptation, distribution and reproduction in any medium or format, as long as you give appropriate credit to the original author(s) and the source, provide a link to the Creative Commons license, and indicate if changes were made. The images or other third party material in this article are included in the article's Creative Commons license, unless indicated otherwise in a credit line to the material. If material is not included in the article's Creative Commons license and your intended use is not permitted by statutory regulation or exceeds the permitted use, you will need to obtain permission directly from the copyright holder. To view a copy of this license, visit <http://creativecommons.org/licenses/by/4.0/>.

© The Author(s) 2019